Experimental extraction of coherent ergotropy and its energetic cost in a superconducting qubit

Li Li [1,2,*] Silu Zhao,[1,2] Yun-Hao Shi [1] Kai Xu [1,3,4] Heng Fan,[1,2,3,4] Dongning Zheng [1,2,4] and Zhongcheng Xiang[1,4,†]
[1]*Beijing National Laboratory for Condensed Matter Physics, Institute of Physics, Chinese Academy of Sciences, Beijing 100190, China*
[2]*School of Physical Sciences, University of Chinese Academy of Sciences, Beijing 100049, China*
[3]*Beijing Academy of Quantum Information Sciences, Beijing 100193, China*
[4]*Hefei National Laboratory, Hefei 230088, China*

(Received 23 June 2025; revised 4 October 2025; accepted 8 November 2025; published 1 December 2025)

Quantum coherence, encoded in the off-diagonal elements of a system's density matrix, is a key resource in quantum thermodynamics, fundamentally limiting the maximum extractable work known as ergotropy. While previous experiments have isolated coherence-related contributions to work extraction, it remains unclear how coherence can be harnessed in a controllable and energy-efficient manner. Here, we experimentally investigate the role of initial-state coherence in work extraction from a superconducting transmon qubit. By preparing a variety of pure states and implementing three complementary extraction protocols, we reveal how coherence governs the partitioning of ergotropy. We find that the choice of initial state depends on the dominant decoherence channel-energy relaxation or dephasing. By further accounting for thermodynamic costs, we identify optimal initial states that maximize the efficiency. Our results demonstrate that the initial-state design provides a scalable approach to coherence control and advances the development of efficient quantum thermodynamic devices.

DOI: 10.1103/ptr1-59tv

I. INTRODUCTION

Quantum batteries (QBs), which are quantum systems designed for energy storage and on-demand release, promise transformative advantages over classical batteries, particularly for scalable, high-efficiency energy transfer [1–19]. A central challenge in QB optimization lies in maximizing the ergotropy, namely, the maximum energy a quantum system can deliver to a work reservoir via cyclic unitary operations [20]. Recent theoretical advances highlight that quantum coherence [21,22] plays a pivotal role in enhancing ergotropy, potentially improving extraction efficiency beyond classical limits [23–27]. This crucial observation was recently confirmed by a pioneering experiment [28], in which the authors used an nitrogen-vacancy (NV) center qubit, gradually dephased a fixed pure state, and observed the corresponding reduction in ergotropy.

However, these findings still leave important questions about how coherence can be effectively harnessed in realistic, controllable settings. In practical systems, decoherence arises from uncontrollable interactions with the environment and represents a fundamentally passive process [29,30]. Although the significance of coherence is well understood, the fact that coherence typically decays passively limits its usefulness for device optimization. In contrast, preparing the initial state of a quantum system is an active process that allows deliberate control and tuning. For quantum energy storage, such active state design is essential to mitigate coherence loss and enhance performance. Consequently, it is necessary to experimentally examine how initial-state coherence impacts work extraction, enabling optimal energy storage strategies. Moreover, the work extraction process consists of a series of unitary operations, each accompanied by thermodynamic cost that can be theoretically quantified [31–34]. Incorporating thermodynamic cost into experimental studies and exploring the relationship between coherence and energy efficiency are also key steps toward optimizing the performance of quantum thermodynamics systems. A critical gap remains: How can we actively design initial states with tailored coherence to optimize ergotropy extraction while minimizing thermodynamic costs?

In this work, we bridge this gap by experimentally investigating how initial-state coherence in a superconducting transmon qubit governs ergotropy extraction and thermodynamic efficiency. First, we implement three distinct work extraction protocols, successfully distinguishing between the coherence-independent and coherence-consuming components of ergotropy. Then, by preparing the qubit in various pure states, we explore how the initial state's coherence affects the relative contributions of these two ergotropy components. We further analyze thermodynamic costs and identify optimal states that maximize preparation efficiency and relate extraction efficiency to coherence. Our results highlight coherence as a key factor in quantum energy storage and conversion, and open a perspective on controlling coherence through initial-state design.

The rest of the paper is organized as follows. In Sec. II, we introduce the concepts of coherent and incoherent ergotropy. In Sec. III, we perform experiments on a superconducting

*Contact author: lilisc05@iphy.ac.cn
†Contact author: zcxiang@iphy.ac.cn

Published by the American Physical Society under the terms of the Creative Commons Attribution 4.0 International license. Further distribution of this work must maintain attribution to the author(s) and the published article's title, journal citation, and DOI.

qubit to extract coherent and incoherent ergotropy. In Sec. IV, we further investigate the proportion of coherent and incoherent ergotropy for different initial states. In Sec. V, we study the thermodynamic loss and efficiency throughout the work extraction process. Finally, we draw our conclusions in Sec. VI.

II. COHERENT AND INCOHERENT ERGOTROPY

We begin with the work extraction cycle of a two-level system, governed by the Hamiltonian $H = H_0 + H_d(t)$. The static part is $H_0 = -\hbar\omega_q\sigma_z/2$, where ω_q is the transition frequency between the ground state $|0\rangle$ and the excited state $|1\rangle$, and $\hbar$ is the reduced Planck constant. The time-dependent term $H_d(t)$ represents external driving, implementing unitary operations for state preparation and work extraction. We prepare the initial state as a pure state $\rho_S = |\psi(\theta)\rangle\langle\psi(\theta)|$, with $|\psi(\theta)\rangle = \cos(\theta/2)|0\rangle + \sin(\theta/2)|1\rangle$, where θ is the Rabi angle corresponding to a Y-axis rotation. This state is illustrated by the black arrow on the Bloch sphere in Fig. 1(a). In this representation, the energy of state ρ_S (denoted by E_{ρ_S}) corresponds to its projection onto the Z axis, while the extractable work is defined as the energy difference between the initial and final states. The ergotropy, the maximum extractable work via unitary evolution U, is given by [20]

$$\mathcal{E}(\rho_S) = \max_U(\mathrm{Tr}[\rho_S H_0] - \mathrm{Tr}[U\rho_S U^\dagger H_0]). \quad (1)$$

The optimal U maps ρ_S to its passive state P_{ρ_S}, from which no work can be further extracted. For a pure state, this passive state is simply the ground state $|0\rangle$, as shown by the downward green arrow in Fig. 1(a), so its ergotropy equals its energy. The ergotropy extraction follows the green arc in Fig. 1(a).

However, mixed states exhibit fundamentally different behavior. We define the fully dephased state of ρ_S as δ_{ρ_S}, obtained via the dephasing process Δ. This state is shown as the upward orange arrow in Fig. 1(a), and Δ is indicated by the orange straight-line trajectory. Its passive counterpart $P_{\delta_{\rho_S}}$ appears as the downward orange arrow. The energy gap between δ_{ρ_S} and $P_{\delta_{\rho_S}}$—i.e., the ergotropy of δ_{ρ_S}—is strictly smaller than that of ρ_S, revealing that coherence, while not affecting energy, determines the amount of extractable work.

The coherence of ρ_S is quantified by the quantum relative entropy [35]

$$C(\rho_S) = D(\rho_S\|\delta_{\rho_S}) = \mathrm{Tr}[\rho_S(\log\rho_S - \log\delta_{\rho_S})], \quad (2)$$

which represents the "distance" between ρ_S and its fully dephased counterpart. The component of ergotropy independent of coherence is termed as *incoherent ergotropy* $\mathcal{E}_i$. It is equivalently defined as the ergotropy of δ_{ρ_S} [orange arc in Fig. 1(a)] or as the maximal work extractable from ρ_S without disturbing its coherence (blue arc). The final state in the latter case, denoted σ_{ρ_S}, is the lowest-energy state preserving the coherence of ρ_S. The operation used to extract the incoherent ergotropy is denoted by V_π, which corresponds to a π rotation around the X axis in the Bloch sphere. The remaining portion of work extractable by consuming coherence is called *coherent ergotropy* $\mathcal{E}_c$, which equals the ergotropy of σ_{ρ_S}, and the operation is denoted by U_c.

For a fixed Rabi angle θ, reducing coherence leads to a monotonic decrease in $\mathcal{E}_c$. A partially dephased state can be

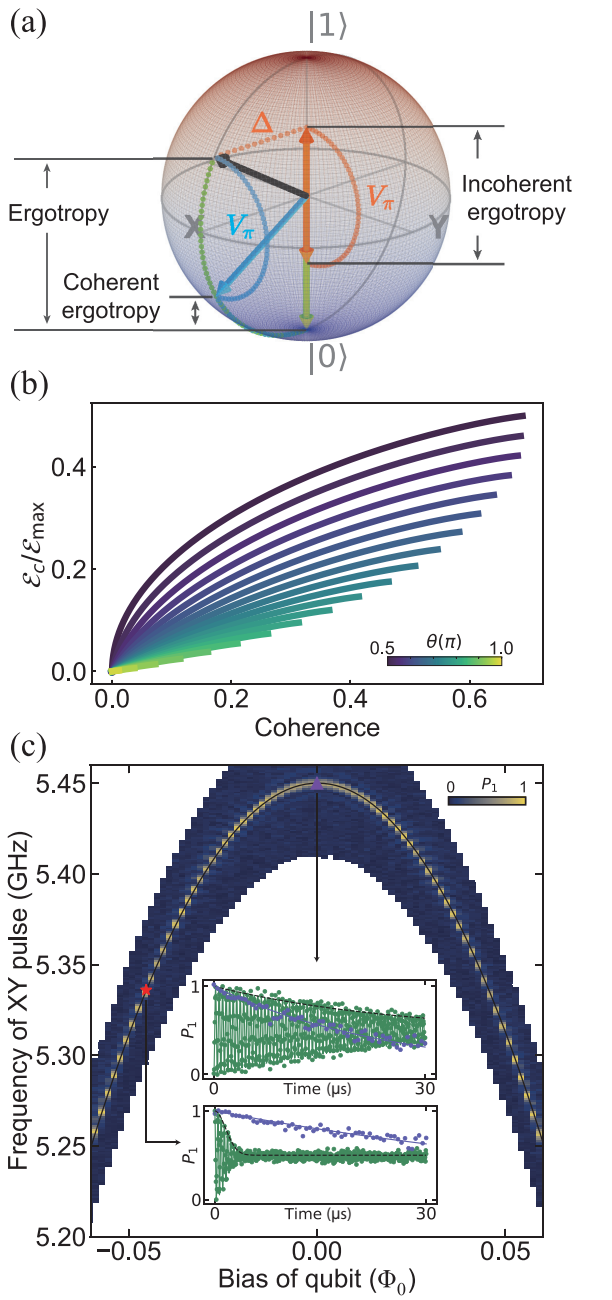


FIG. 1. Coherent and incoherent ergotropy in a superconducting qubit. (a) Bloch sphere representation of ergotropy extraction from a pure state $\rho_S = |\psi(\theta)\rangle\langle\psi(\theta)|$ (black arrow). The ergotropy $\mathcal{E}(\rho_S)$ corresponds to the green arc to the ground state (passive state). Dephasing Δ yields the mixed state δ_{ρ_S} (upward orange arrow), whose ergotropy is the orange arc. The blue arc denotes incoherent ergotropy—the maximal work extractable without consuming coherence—ending in σ_{ρ_S}. The remainder, coherent ergotropy, is extractable via a unitary U_c. (b) Coherent ergotropy as a function of coherence and Rabi angle θ. It increases with coherence at fixed θ, and depends on θ due to gate-induced coherence. (c) Experimental implementation using a transmon qubit. $\Phi_0 = h/2e$ is the flux quantum, where e is the elementary charge and h is Planck's constant. The flux dependence of the qubit frequency ω_q shows a sweet spot (purple triangle) with long dephasing time $T_2 = 32.7\,\mu$s and short $T_1 = 25.7\,\mu$s, and a detuned point (red star) with $T_2 = 2.2\,\mu$s and $T_1 = 64.5\,\mu$s, enabling preparation of δ_{ρ_S}.

written as

$$\rho_S^{\Delta} = \begin{bmatrix} \sin^2(\theta/2) & a \\ a^* & \cos^2(\theta/2) \end{bmatrix}, \tag{3}$$

where $|a| \leqslant \sin(\theta/2)\cos(\theta/2)$ controls the residual coherence. The coherence $C(\rho_S^{\Delta})$ dependence with a quantifies the degree of phase information. Figure 1(b) shows that $\mathcal{E}_c$ increases with $C(\rho_S^{\Delta})$ for a fixed θ. Besides, Fig. 1(b) further reveals how $\mathcal{E}_c$ depends on the Rabi angle varying between $\pi/2$ and π. This effect is nontrivial: The available coherence resource directly stems from the unitary gate used during initialization. In large-scale QBs, such dependencies influence charging power and efficiency. We now investigate this phenomenon using a superconducting transmon qubit [36].

III. WORK EXTRACTION PROTOCOLS FOR SUPERCONDUCTING QUBIT

To experimentally distinguish coherent and incoherent ergotropy, it is essential to prepare the relevant intermediate quantum states. The most challenging among them is the mixed state δ_{ρ_S}, requiring implementation of Δ: fast suppression of off-diagonal elements while preserving diagonal populations. The mixed-state preparation is closely related to noise engineering and plays an important role in open-system quantum simulation [37–46]. In superconducting circuits, one approach introduces auxiliary systems—qubits or resonators—to induce controllable dissipation [42,46], but this demands custom hardware. Alternatively, one can apply engineered noise via the qubit's control lines, e.g., random XY noise [39] or synthesized low-frequency Z noise [40,41]. However, XY noise typically drives the system to a unique steady state, unsuitable for our purposes. Z-noise-based dephasing is often limited by device quality, which must ensure spectrally clean relaxation dynamics free of two-level defects [47–52].

In this study, we exploit the qubit's intrinsic environment to induce dephasing. Figure 1(c) shows the dependence of a transmon qubit's transition frequency on magnetic flux Φ. The point marked by the purple triangle is the transmon's sweet spot, where $\omega_q^s/2\pi = 5.450\,\text{GHz}$ and $\partial\omega_q/\partial\Phi = 0$. This location is immune to flux noise and yields a long dephasing time, $T_2 = 32.7\,\mu\text{s}$. However, it is also closest to the readout resonator frequency, resulting in strong Purcell decay and a short energy relaxation time, $T_1 = 25.7\,\mu\text{s}$. Conversely, the red star marks a flux bias point with the opposite trade-off $\omega_q/2\pi = 5.336\,\text{GHz}$, $T_1 = 64.5\,\mu\text{s}$ and $T_2 = 2.2\,\mu\text{s}$. These parameters are well suited for implementing Δ and preparing δ_{ρ_S}. The drive is applied through the XY control line. The drive Hamiltonian takes the form $H_d(t) = g_d v(t)\cos(\omega_d t)\sigma_y$, where g_d is the drive-qubit coupling strength, $v(t)$ is the time-dependent envelope, and ω_d is the frequency of drive. We take $\omega_d = \omega_q$ in the following experiment. Figure 2 presents the experimental results for three distinct work extraction protocols, which we refer to as dephasing extraction, direct extraction, and sequential extraction. In all cases, the initial state is the pure state $\rho_S = |\psi_0\rangle\langle\psi_0|$, $|\psi_0\rangle = (\sqrt{2}|1\rangle + |0\rangle)/\sqrt{3}$, with a Rabi angle $\theta_S = 2\arccos(\sqrt{3}/3)$. The final states are reconstructed via quantum state tomography to obtain their full density matrices [53,54]. Figure 2(a) illustrates the state preparation outcomes on the Bloch sphere. For all protocols, state preparation is repeated 20 times, with the results plotted as individual points. The corresponding average Bloch vectors are shown as arrows. Figure 2(b) quantifies the relationship between coherence and energy for each state, where all energies are normalized to the maximum energy scale, $E_{\max} = \hbar\omega_q$.

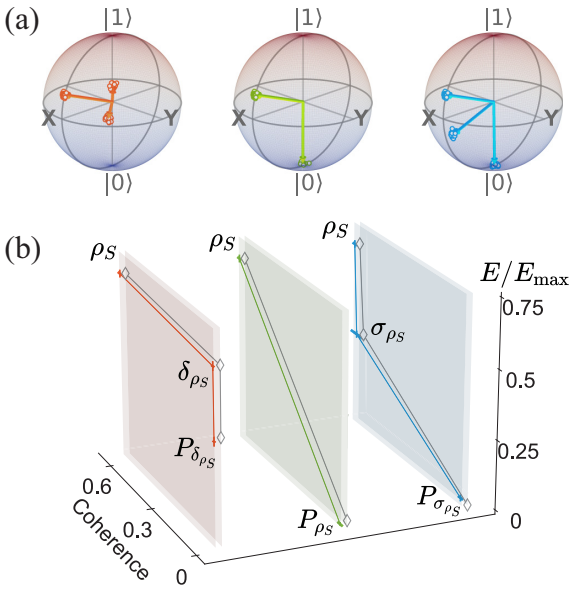


FIG. 2. Experimental comparison of three work extraction protocols from a superconducting qubit. (a) Bloch sphere representation of quantum states under dephasing extraction (orange), direct extraction (green), and sequential extraction (blue). Dots indicate individual state preparations; arrows show average Bloch vectors. (b) Energy-coherence diagram for the extracted states. Each trajectory illustrates how energy and coherence are reduced under different protocols. The error bars represent the standard error. Gray diamonds represent numeric simulation results accounting for all decoherence effects.

In the dephasing extraction protocol, the initial state ρ_S is held at the working point for 4 μs, during which phase decoherence suppresses all off-diagonal elements, yielding the fully dephased state δ_{ρ_S}. A subsequent application of the V_π operation transforms δ_{ρ_S} into its passive state $P_{\delta_{\rho_S}}$. The experimental results for this process are shown in orange in both Figs. 2(a) (left side) and 2(b) (left path). The $\mathcal{E}_i$ extracted in this protocol is found to be 0.26 ± 0.02. In the direct extraction protocol, the total ergotropy of ρ_S is extracted via a single unitary operation that is the inverse of the state preparation gate. The corresponding results are shown in green in the center of Figs. 2(a) and 2(b). The sequential extraction protocol decomposes the process into two steps. First, a V_π operation is applied to ρ_S, producing the state σ_{ρ_S} and extracting the $\mathcal{E}_i$, measured to be 0.33 ± 0.02. Second, the remaining coherence is consumed by transforming σ_{ρ_S} into its passive state $P_{\sigma_{\rho_S}}$ by U_c, extracting the, $\mathcal{E}_c$ which is 0.34 ± 0.01. These operations are represented by the blue states and trajectories on the right side of Figs. 2(a) and 2(b). The discrepancy in $\mathcal{E}_i$ between the dephasing and sequential protocols arises from unavoidable decay of the population terms during the dephasing process

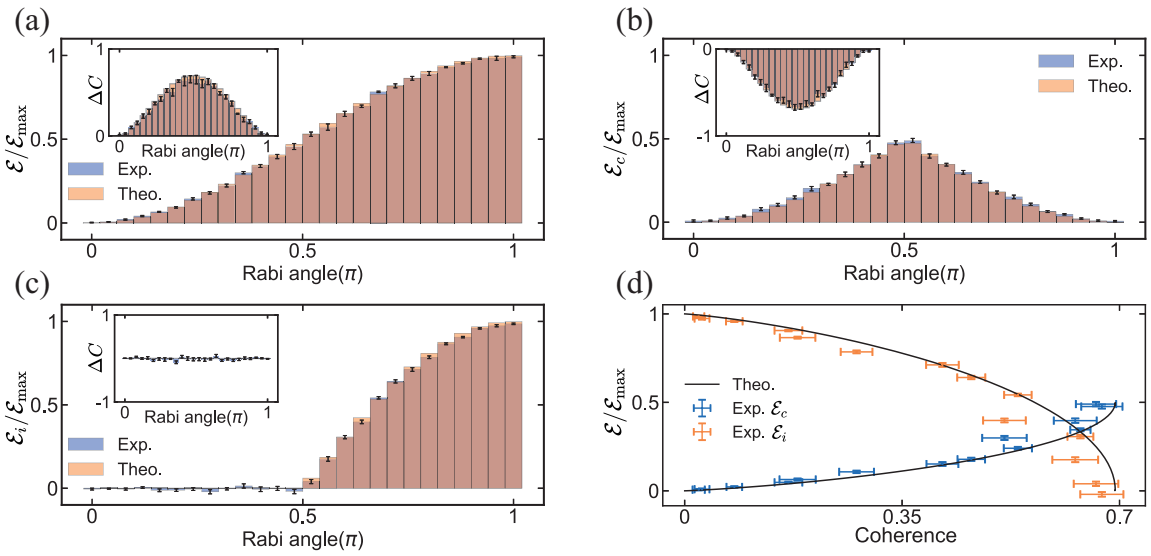


FIG. 3. Variation of ergotropy and coherence in the sequential protocol as a function of the Rabi angle θ. (a) Change in $\mathcal{E}$ and coherence ΔC of the prepared state ρ_θ relative to the ground state. The blue bars represent experimental data, and the brown bars represent theoretical calculations. (b) Coherent ergotropy $\mathcal{E}_c$ vs θ; the inset shows the coherence drop after coherent extraction during U_c, indicating full consumption. (c) Incoherent ergotropy $\mathcal{E}_i$ as a function of θ, becoming dominant near $\theta = \pi$. The inset shows coherence remaining unchanged during V_π. (d) Initial coherence $C(\rho_\theta)$ plotted against $\mathcal{E}_c$ and $\mathcal{E}_i$, revealing their respective positive and negative correlations with coherence. The black solid line represents the theoretical calculation. All error bars represent the standard error.

Δ. To model this quantitatively, we simulate the full ergotropy extraction dynamics using the measured decoherence parameters of the superconducting qubit and numerically solve the master equation with qutip [55,56]. The results, plotted as gray diamond markers in Fig. 2(b), show good agreement with experimental data. These findings demonstrate the experimental distinction between coherent and incoherent ergotropy on a superconducting qubit and confirm the dependence of coherent ergotropy on the amount of quantum coherence.

IV. COHERENT AND INCOHERENT ERGOTROPY FOR DIFFERENT INITIAL STATES

We prepare initial states with varying Rabi angles θ for the sequential extraction protocol and denote the extracted changes in energy and coherence during the process. Figure 3(a) shows the state preparation results as θ varies from 0 to π, the corresponding operation is denoted as $R_Y(\theta)$. The energy changes from the ground state to ρ_θ is $\sin^2(\theta/2)\hbar\omega_q$, and the coherence is $-2\sin^2(\theta/2)\log(\sin(\theta/2)) - 2\cos^2(\theta/2)\log(\cos(\theta/2))$. When $\theta < \pi/2$, the state ρ_θ itself is passive with the same coherence. Therefore, the $\mathcal{E}_i$ is zero and all extractable work is coherent. For $\pi/2 < \theta < \pi$, we apply a V_π operation to prepare σ_{ρ_θ} and then perform coherent work extraction to prepare $P_{\sigma_{\rho_\theta}}$. Figure 3(b) displays the coherent ergotropy versus θ, which reaches a maximum of 0.5 at $\theta = \pi/2$. The inset of Fig. 3(b) shows the coherence difference before and after coherent extraction, indicating full coherence consumption. Subtracting $\mathcal{E}_c$ from total work yields the $\mathcal{E}_i$ as a function of θ, shown in Fig. 3(c). At $\theta = \pi$, all work is incoherent. Figure 3(d) plots the initial coherence against coherent (incoherent) ergotropy, confirming the positive (negative) correlation. This guides optimal charging of QBs: In systems dominated by phase decoherence such as superconducting, NV centers, or spins qubits, energy should be stored incoherently by preparing $\theta = \pi$. When dynamical decoupling [57–63] extends dephasing time $T_2 \simeq 2T_1$, coherent storage with $\theta = \pi/2$ is preferable.

V. THERMODYNAMIC EFFICIENCY OF STATE PREPARATION AND WORK EXTRACTION

Finally, we analyze the thermodynamic cost and efficiency associated with each step of the sequential extraction protocol. For a unitary quantum gate of duration τ, the thermodynamic cost can be expressed as [33,34,64–66]

$$\Sigma = \frac{1}{\tau}\int_0^\tau \|H_d(t)\|\mathrm{d}t, \tag{4}$$

where $\|H_d(t)\|$ denotes the operator norm of $H_d(t)$. In our experiment, each unitary step is implemented over a fixed duration of 80 ns. The integration in Eq. (14) can be written as $\int_0^\tau g_d v(t)\mathrm{d}t$, which corresponds precisely to the definition of the Rabi angle θ and is independent of the pulse envelope.

Combining thermodynamic cost with the energy change ΔE, we define the thermodynamic efficiency as $\eta = \Delta E/(\Delta E + \Sigma)$. For the state preparation step, ΔE denotes the energy stored; for the extraction steps, it represents the amount of extracted work. Figure 4 shows the efficiencies of $R_Y(\theta)$, V_π, U_c, and total extraction processes (Total) as functions of $C(\rho_\theta)$. The corresponding Rabi angles range from $\pi/2$ to π. The efficiency of coherent ergotropy extraction increases monotonically with coherence, since coherent ergotropy grows with coherence, while the thermodynamic cost decreases. Conversely, the efficiencies of incoherent and total ergotropy extraction processes decrease with increasing coherence.

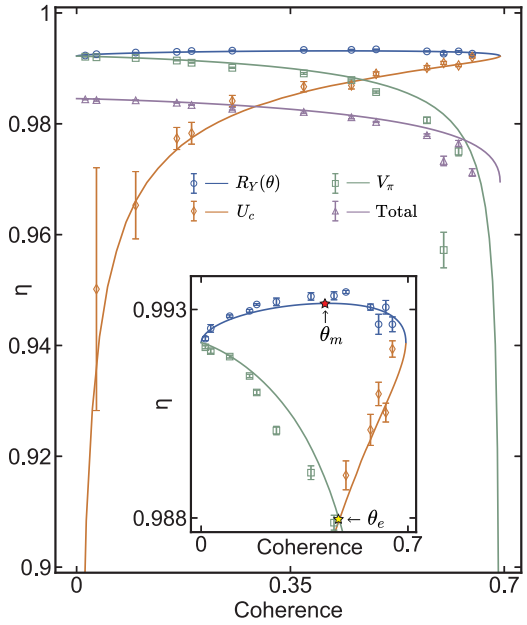


FIG. 4. Thermodynamic efficiencies η of state preparation $R_Y(\theta)$, coherent extraction U_c, incoherent extraction V_π, and total extraction vs coherence $C(\rho_\theta)$. The inset marks a local maximum preparation efficiency at $\theta_m \approx 0.742\pi$ with $C_m \approx 0.432$ and equal extraction efficiencies at $\theta_e \approx 0.722\pi$ with $C_e \approx 0.469$. The error bars represent the standard error.

Three features emerge from the results. First, the preparation efficiency exhibits a local maximum at a Rabi angle $\theta_m \approx 0.742\pi$ and coherence $C_m \approx 0.432$, marked by a red star in the inset. This indicates an optimal energy-to-cost ratio for charging the QB in the absence of decoherence. Combined with the results of Fig. 3, this suggests a trade-off between maximum efficiency and maximum ergotropy lifetime in realistic battery operation. Second, at $\theta_e \approx 0.722\pi$, the efficiencies of coherent and incoherent ergotropy extraction are equal, corresponding to coherence $C_e \approx 0.469$, marked by a yellow star in the inset. Notably, this does not imply equal amounts of $\mathcal{E}_c$ and $\mathcal{E}_i$, but rather equal efficiency due to the combined effects of work and thermodynamic cost. Third, when coherence reaches its maximum or minimum, the coherent (incoherent) ergotropy extraction efficiency matches that of state preparation, forming a closed curve in the efficiency-coherence plane. This occurs because in these limits, all ergotropy is coherent (incoherent), and the corresponding operations U_C (V_π) are the inverse of $R_Y(\theta)$.

VI. CONCLUSION

In summary, we have experimentally resolved coherent and incoherent ergotropy in a superconducting transmon qubit using three distinct work extraction protocols. Our results provide the first experimental verification on a superconducting qubit platform that, while quantum coherence does not alter the energy of a state, it fundamentally determines the amount of extractable work [23–26]. By varying the Rabi angle of the initial state, we observe a clear positive correlation between coherence and coherent ergotropy, and a negative correlation for incoherent ergotropy. This suggests that the choice of initial state can be optimized based on the decoherence characteristics of the QBs—for instance, storing coherent ergotropy to avoid energy relaxation or storing incoherent ergotropy to avoid dephasing. Furthermore, by analyzing the thermodynamic cost and efficiency of each step in the extraction cycle, we identify an optimal initial state that maximizes the charging efficiency. Altogether, our findings highlight a fundamental trade-off between coherence and efficiency in quantum energy storage, offering practical guidance for improving the performance of quantum devices. Future work could extend these concepts to multiqubit systems, exploring how coherence-based strategies generalize in the presence of entanglement, laying the groundwork for scalable QBs. Additionally, we have systematically compared several methods of mixed-state preparation. These methods are platform-independent and, beyond quantum thermodynamics, can also be applied to quantum simulations of open systems [37] or non-Hermitian systems [67].

ACKNOWLEDGMENTS

This work was supported by the Micro/Nano Fabrication Laboratory of Synergetic Extreme Condition User Facility (SECUF). The devices were made at the Nanofabrication Facilities at the Institute of Physics, CAS in Beijing. This work was supported by Quantum Science and Technology-National Science and Technology Major Project (Grant No. 2021ZD0301800), the National Natural Science Foundation of China (Grants No. 12204528, No. 92265207, No. T2121001, No. 92065112, No. 92365301, No. T2322030, and No. 12504593).

DATA AVAILABILITY

The data that support the findings of this article are not publicly available. The data are available from the authors upon reasonable request.

APPENDIX A: DEVICE AND MEASUREMENT SETUP

Figure 5 shows the optical micrograph of the superconducting transmon (Xmon) qubit [36,68] used in this work, fabricated from aluminum thin film on a high-resistivity sapphire substrate. The Josephson junctions, forming a superconducting quantum interference device (SQUID) loop at the bottom of the qubit capacitor, are realized using double-angle evaporation of aluminum with an intermediate oxidation step to form the Al/AlOx/Al tunnel barriers. Capacitors, control lines, and readout resonators are defined by optical lithography and patterned via wet etching.

The qubit capacitor, highlighted in blue, consists of a cross-shaped structure that provides strong charge-noise protection while setting the qubit's charging energy. The SQUID loop enables tunability of the qubit frequency via magnetic flux biasing. The readout cavity, shown in green, is a zigzag $\lambda/4$ coplanar waveguide resonator that couples dispersively to the qubit. The transmission line (in red) is coupled to the readout cavity and used for resonator transmission measurements.

Two control lines are used for qubit manipulation: The XY control line (in orange), which delivers microwave drive

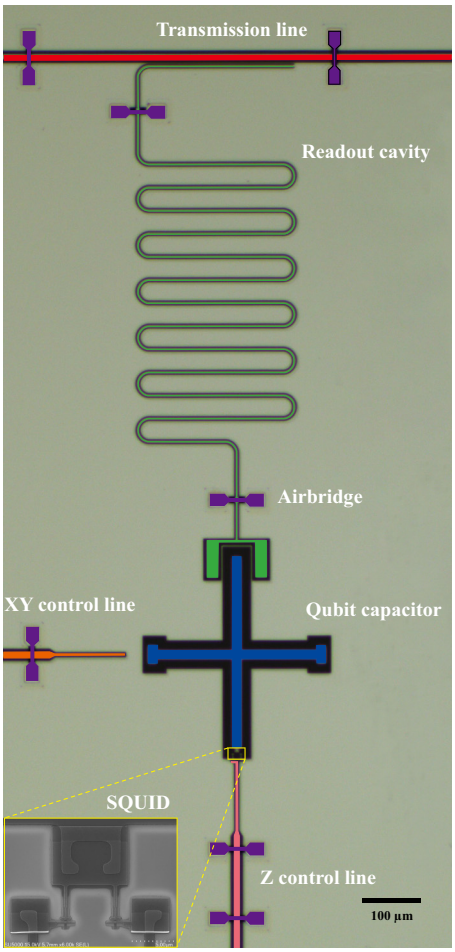


FIG. 5. False-colored optical micrograph of the superconducting Xmon qubit device used in this experiment. The cross-shaped capacitor (blue) sets the charging energy and helps suppress charge noise, while the SQUID loop allows frequency tunability through flux bias. The $\lambda/4$ readout resonator (green) capacitively couples to the qubit and is accessed via the transmission line (red). Qubit control is achieved using an XY line (orange) for microwave drives and a Z line (magenta) for fast flux tuning. Airbridges (purple) maintain ground continuity and suppress slotline modes in the coplanar geometry.

pulses for coherent control of the qubit state, and the Z control line (in magenta), which applies flux bias to tune the qubit frequency. Airbridges (in purple) are employed to suppress parasitic slotline modes by ensuring ground continuity across the coplanar waveguide structures.

Our experimental setup shares the same control architecture and cryogenic wiring as our previous work [69], with the exception that no DC bias line is used. The XY control signal is generated by mixing a continuous-wave microwave tone with modulated wave forms from an arbitrary wave form generator using an in-phase/quadrature (IQ) mixer, enabling precise control over qubit rotations. The Z control consists of two components: a slow bias Z signal that emulates the effect of a DC bias and a fast Z signal used to dynamically modulate the qubit frequency. These XY and Z signals are combined at room temperature and sent through Z control line (XY control line is not used). The signal path is equipped with attenuators and filters at different temperature stages to suppress noise.

For single-qubit state readout, a microwave tone is sent to the readout resonator and the reflected signal is amplified by a cryogenic high electron mobility transistor amplifier and further processed at room temperature. The demodulated signal is digitized by an analog-to-digital converter. Due to the high readout fidelity achieved in our chip, no Josephson parametric amplifier is required.

APPENDIX B: MIXED STATE PREPARATION

1. Engineered XY noise

An efficient method for preparing mixed states is to use discrete random noise [39]. For a single-qubit system with density matrix ρ, the environmental effects can be modeled as comprising two parts: delay and pump, described by the Lindblad operators σ_- and σ_+, respectively. The corresponding rates are denoted by γ_- and γ_+. The master equation takes the form

$$\dot{\rho} = -i[H_0, \rho] + \gamma_- \mathcal{D}[\sigma_-]\rho + \gamma_+ \mathcal{D}[\sigma_+]\rho, \tag{B1}$$

where H_0 is the system Hamiltonian, $\mathcal{D}[A]\rho = A\rho A^\dagger - \frac{1}{2}\{A^\dagger A, \rho\}$ denotes the standard Lindblad superoperator. If $\gamma_- = \gamma_+ = \gamma$, the master equation can be written as

$$\dot{\rho} = -i[H_0, \rho] + \frac{\gamma}{2}\mathcal{D}[\sigma_x]\rho + \frac{\gamma}{2}\mathcal{D}[\sigma_y]\rho. \tag{B2}$$

It is equivalent to a stochastic Schrodinger equation

$$\begin{aligned} i\frac{d}{dt}|\psi\rangle &= H_S(t)|\psi\rangle, \\ H_S(t) &= H_0 + \sqrt{\gamma}\eta_1(t)\sigma_x + \sqrt{\gamma}\eta_2(t)\sigma_y \\ &= H_0 + \tilde{H}(t). \end{aligned} \tag{B3}$$

Due to the sampling rate of the device, we use Euler method for this random process, assuming the time interval is δt:

$$|\psi\rangle_{t+1} = \exp(-iH_0\delta t + \tilde{H}(t)\eta_t\sqrt{\delta t})|\psi\rangle_t, \tag{B4}$$

where η_t is a random variable satisfying $\overline{\eta_t} = 0$, $\overline{\eta_t^2} = 1$. Using Taylor's formula, we get

$$|\psi\rangle_{t+1} = \exp(-i\tilde{H}_T(t)\delta t)|\psi\rangle_t, \tag{B5}$$

$$\tilde{H}_T(t) = H_0 + \frac{\tilde{H}(t)}{\sqrt{\delta t}}. \tag{B6}$$

The $\tilde{H}_T(t)$ to be implemented becomes

$$\tilde{H}_T(t) = \sqrt{\frac{\gamma}{\delta t}}\eta_1(t)\sigma_x + \sqrt{\frac{\gamma}{\delta t}}\eta_2(t)\sigma_y. \tag{B7}$$

In each δt, the Hamiltonian is time independent:

$$\tilde{H}_T = \sqrt{\frac{\gamma}{\delta t}}\eta_1\sigma_x + \sqrt{\frac{\gamma}{\delta t}}\eta_2\sigma_y. \tag{B8}$$

To implement the dynamics described by the master equation, we emulate the corresponding Hamiltonian using a sequence of discrete stochastic pulses, thereby driving the pure state into a mixed state under controlled evolution. In the experiment, we first characterize the statistical properties

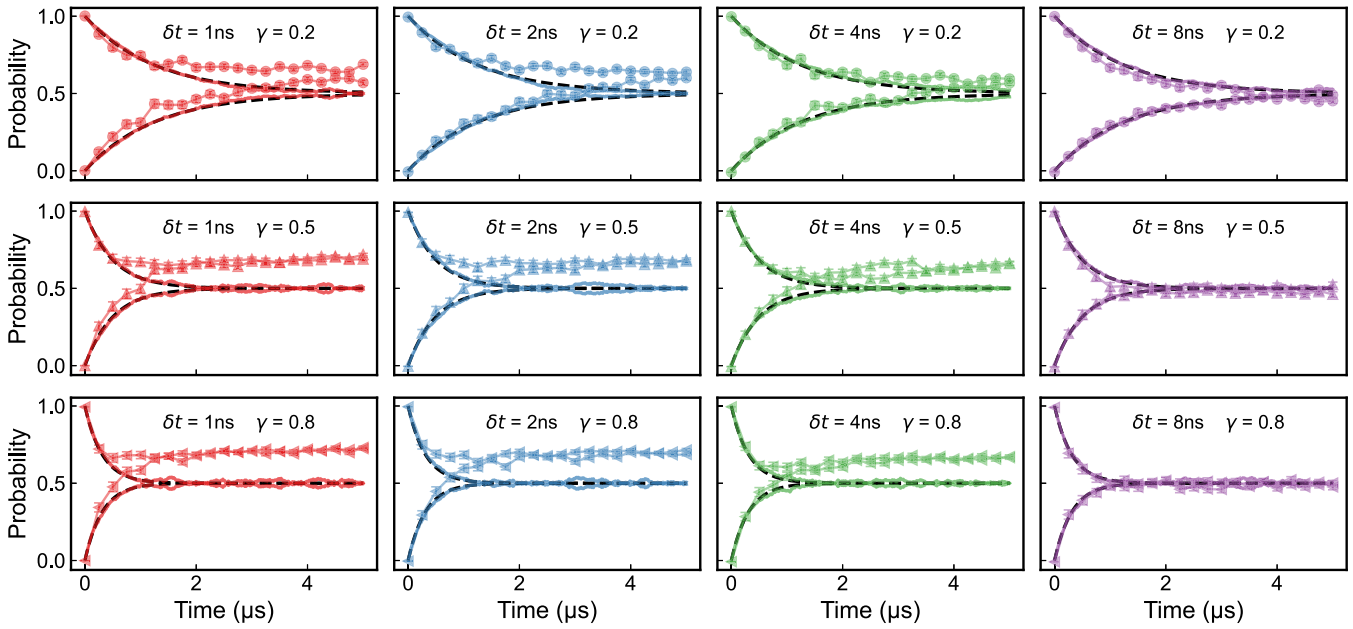


FIG. 6. The δt and γ calibration of the engineered XY noise. The qubit is prepared initially in either the ground state $|0\rangle$ or the excited state $|1\rangle$, and subsequently evolves under stochastic noise with the corresponding parameters. Data points represent experimental results, solid lines correspond to numerical simulations of the stochastic Schrodinger equation [Eq. (B6)], and the black dashed lines denote simulations of the master equation [Eq. (B2)]. When δt is below 8 ns, the curves exhibit an upward deviation in the steady state due to pulse distortion and leakage to higher energy levels. At $\delta t = 8$ ns, the experimental data and numerical simulations show good agreement.

of the applied random noise under various values of δt and γ. Specifically, the qubit is initialized in either the $|0\rangle$ or $|1\rangle$ state and then subjected to stochastic evolution along multiple noise trajectories. For each parameter setting, we average the outcomes over 50 independent trajectories. Our random sequence follows a Bernoulli distribution, ensuring consistent binary sampling in each interval. Figure 6 shows the averaged results for each parameter set.

As shown in Fig. 6, when $\delta t < 8$ ns, the steady-state results deviate significantly from numerical simulations. In contrast, good agreement is observed at $\delta t = 8$ ns. This discrepancy arises from two primary factors. First, the random pulses generated by the arbitrary wave form generator exhibit large amplitude discontinuities, which introduce distortions both at the source and along the cryogenic transmission lines. Second, shorter pulse intervals lead to broader spectral components, increasing the probability of exciting the weakly anharmonic transmon to higher energy levels. Based on these considerations, we choose a step size of 8 ns for the subsequent experiments.

We next prepare the qubit in the superposition state $(|0\rangle + |1\rangle)/\sqrt{2}$ to evaluate the effectiveness of random noise in generating mixed states. Figure 7(a) shows the time evolution of the diagonal and off-diagonal elements of the density matrix under random pulses for various noise strengths $\gamma = 0.5$, 0.8, 1.2, and 2.0. As γ increases, the off-diagonal elements decay more rapidly, vanishing within 1 μs. In contrast, the diagonal elements remain near 0.5 throughout the measurement window, showing no significant variation. Figure 7(b) displays the evolution of the state's coherence, which decays rapidly under noise. Owing to its definition, the coherence signal exhibits weaker oscillations compared to the individual matrix elements. These results demonstrate both the efficacy and tunability of random XY noise in preparing mixed quantum states.

However, this method also has a clear limitation: It can only generate the maximally mixed state, since the steady-state solution of the Eq. (B2) converges to the fully mixed state. As a result, when implementing the Δ process corresponding to the initial state ϕ_S in the main text, we did not adopt the engineered XY-noise method.

2. Engineered Z noise

In Refs. [40,41], the authors simulate low-frequency noise by applying random bias fluctuations through the Z control channel, thereby preparing mixed states. This method is conceptually simple and easy to implement, as illustrated in Fig. 10(b). However, it places stringent requirements on the qubit's T_1 across a wide frequency range near its work point, since the protocol effectively applies uniform delays over the entire frequency band. In our device, a significant number of two-level defects are present, as shown in Fig. 8(a). As a result, while the Z-randomization method can efficiently suppress the off-diagonal elements, it also causes rapid decay of the diagonal terms.

3. Intrinsic environmental noise

In this work, we utilize the qubit's intrinsic physical environment to prepare mixed states. Figure 8 shows the measured T_1 and T_2 of the qubit as functions of the transition frequency. While T_2 exhibits strong frequency dependence, T_1 is more sensitive to the presence of two-level defects in the surrounding frequency environment. We choose $\omega_q/2\pi = 5.336$ GHz as the working point to induce off-diagonal decay. The corre-

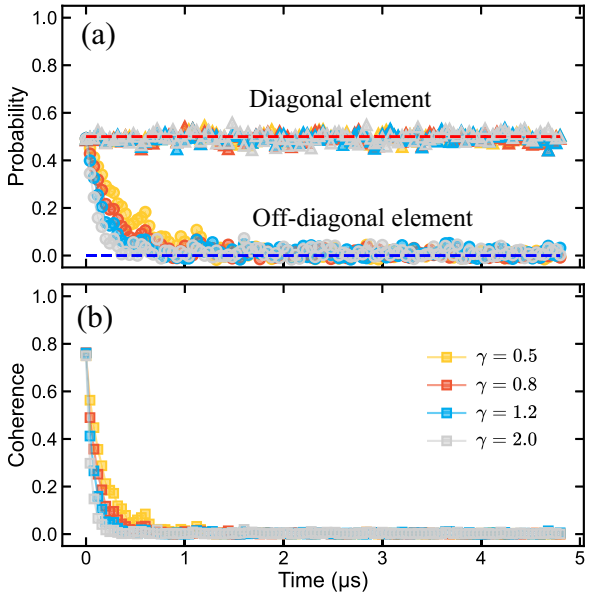


FIG. 7. Decay of the qubit population and coherence under engineered *XY* noise, with the qubit initially prepared in the superposition state $(|0\rangle + |1\rangle)/\sqrt{2}$. (a) Diagonal and off-diagonal elements of the qubit density matrix reconstructed via quantum state tomography. The red dashed line indicates the steady-state population value of 0.5, and the blue dashed line indicates the steady-state coherence value of 0. (b) Qubit coherence calculated from the density matrix. These results demonstrate the tunability of the engineered *XY*-noise strength. In both (a) and (b), yellow, red, blue, and gray lines correspond to $\gamma = 0.5$, 0.8, 1.2, and 2.0, respectively.

sponding test experimental results are presented in Fig. 9. The qubit is initialized in the superposition state $(|0\rangle + |1\rangle)/\sqrt{2}$, followed by a fast Z pulse that shifts its frequency to the working point. After a controlled delay, quantum state tomography is performed to reconstruct the density matrix. As shown in Fig. 9(a), the off-diagonal elements decay rapidly with increasing delay time and reach a steady state at approximately 4 μs. In contrast, the diagonal elements exhibit minimal decay. Figure 9(b) plots the qubit coherence as a function of delay time, confirming that the qubit has lost all coherence by 4 μs.

We compare the principles of three mixed-state preparation methods, illustrated schematically in Fig. 10.

APPENDIX C: PULSE SEQUENCE

Figure 11 illustrates the pulse sequences for the three types of work extraction processes discussed in the main text: sequential extraction, dephasing-assisted extraction, and direct extraction. All XY channel pulses have the same duration of 80 ns. The rotation angle is controlled by the pulse amplitude, and the rotation axis is determined by the pulse phase.

APPENDIX D: COHERENCE AND ERGOTROPY

1. Single qubit operation

The total Hamiltonian is ($\hbar = 1$)

$$H = -\frac{\omega_q}{2}\sigma_z + g_d V(t)\sin(\omega_d t + \varphi)\sigma_y = H_0 + H_d, \quad \text{(D1)}$$

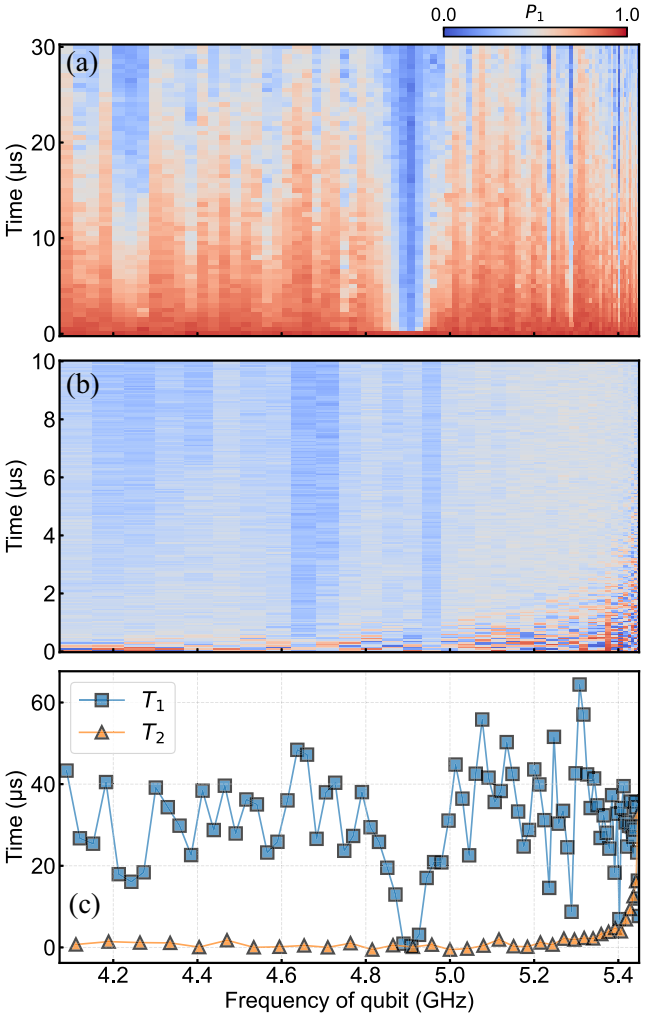


FIG. 8. The qubit's energy relaxation and dephasing properties as functions of transition frequency. (a) Energy relaxation sequence: The qubit is prepared in the excited state $|1\rangle$, biased to a specific frequency, delayed for a certain time, and then the remaining population in $|1\rangle$ is measured. (b) Ramsey sequence: The qubit is prepared in state $\frac{1}{\sqrt{2}}(|0\rangle + |1\rangle)$, biased to a specific frequency, delayed, then an $X/2$ rotation is applied before measuring the off-diagonal element. (c) The dependence of the qubit's T_1 and T_2 on transition frequency. T_1 is extracted by fitting the decay in panel (a) with $P_1 = Ae^{-t/T_1} + B$, and T_2 is extracted by fitting the Ramsey decay in panel (b) with $P_1 = Ae^{-t/T_2}\cos(\omega_1 t + \phi) + B$.

where g_d denotes the coupling strength between the qubit and the control line and $V(t)$ is the envelope of the control field. Defining a rotating frame transformation

$$U_{rf} = \exp\left(-i\frac{\omega_d}{2}\sigma_z t\right), \quad \text{(D2)}$$

the interaction Hamiltonian can be written as

$$H_I = U_{rf}H_0U_{rf}^\dagger + U_{rf}H_dU_{rf}^\dagger - iU_{rf}\frac{\partial U_{rf}^\dagger}{\partial t}. \quad \text{(D3)}$$

Thus, we get the propagator

$$U_P(t) = e^{-iH_I t} = \cos\left(\frac{\Omega_R t}{2}\right)I - i\sin\left(\frac{\Omega_R t}{2}\right)\frac{2H_I}{\Omega_R}. \quad \text{(D4)}$$

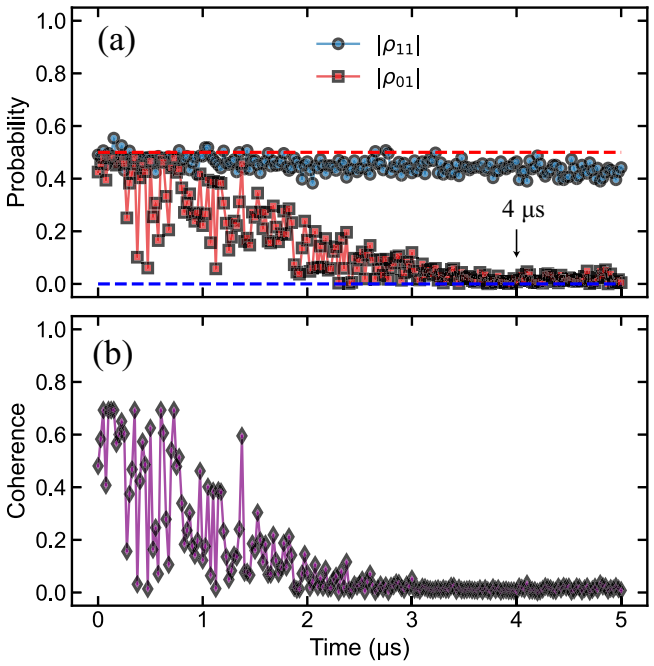


FIG. 9. Mixed-state preparation via intrinsic environmental noise. The qubit is initialized in the superposition state $(|0\rangle + |1\rangle)/\sqrt{2}$. (a) Decay of the off-diagonal elements (red squares) and diagonal elements (blue circles) of the density matrix. (b) Decay of coherence. The coherence vanishes completely after approximately 4 μs.

From the initial state $|g\rangle$, the final state $|\psi(t)\rangle$ is

$$\begin{aligned}|\psi(t)\rangle &= U_P(t)|g\rangle \\ &= \left[\cos\left(\frac{\Omega_R t}{2}\right) + i\frac{\Delta}{\Omega_R}\sin\left(\frac{\Omega_R t}{2}\right)\right]|g\rangle \\ &\quad + \left[-i\frac{\Omega_0}{\Omega_R}\sin\left(\frac{\Omega_R t}{2}\right)\right]|e\rangle. \end{aligned} \tag{D5}$$

The probability

$$\begin{aligned}P_g &= \left|\cos\left(\frac{\Omega_R t}{2}\right) + i\frac{\Delta}{\Omega_R}\sin\left(\frac{\Omega_R t}{2}\right)\right|^2 \\ &= 1 - \frac{\Omega_0^2}{\Omega_R^2}\sin^2\left(\frac{\Omega_R t}{2}\right), \\ P_e &= \left|-i\frac{\Omega_0}{\Omega_R}\sin\left(\frac{\Omega_R t}{2}\right)\right|^2 \\ &= \frac{\Omega_0^2}{\Omega_R^2}\sin^2\left(\frac{\Omega_R t}{2}\right). \end{aligned} \tag{D6}$$

Under the resonate condition ($\Delta = 0$), we obtain

$$\begin{aligned}P_g &= \cos^2\left(\frac{\Omega_0 t}{2}\right), \\ P_e &= \sin^2\left(\frac{\Omega_0 t}{2}\right). \end{aligned} \tag{D7}$$

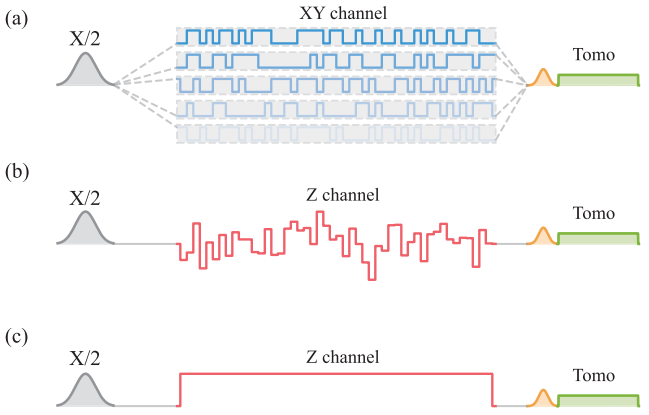


FIG. 10. The principles of three mixed-state preparation methods that require no auxiliary hardware. (a) Engineered XY noise. This approach simulates a stochastic Schrödinger equation using randomly sampled pulse sequences, effectively mapping XY control into a tunable dissipative channel. (b) Engineered Z noise. Here, random frequency shifts are introduced via Z pulses, emulating the effect of low-frequency noise through stochastic detuning. (c) Intrinsic environmental noise. The qubit evolves under its natural physical environment, positioned at a frequency point with strong pure dephasing but minimal energy relaxation, to induce coherence decay.

The density matrix $\rho = |\psi\rangle\langle\psi|$ is ($|e\rangle = \binom{1}{0}$, $|g\rangle = \binom{0}{1}$)

$$\rho_S = \begin{bmatrix} \sin^2\left(\frac{\Omega_0 t}{2}\right) & i\sin\left(\frac{\Omega_0 t}{2}\right)\cos\left(\frac{\Omega_0 t}{2}\right) \\ -i\sin\left(\frac{\Omega_0 t}{2}\right)\cos\left(\frac{\Omega_0 t}{2}\right) & \cos^2\left(\frac{\Omega_0 t}{2}\right) \end{bmatrix}. \tag{D8}$$

If $\dot{V}(t) \neq 0$, Eq. (D7) can be expanded as

$$\begin{aligned}P_g &= \cos^2\left(\int_0^t \frac{g_d V(\tau)}{2} d\tau\right), \\ P_e &= \sin^2\left(\int_0^t \frac{g_d V(\tau)}{2} d\tau\right). \end{aligned} \tag{D9}$$

2. $\mathcal{E}$ versus Rabi angle

For the pure state $|\psi\rangle$, define the Rabi angle θ as $\int_0^t g_d V(\tau)$, which physically corresponds to the angular displacement between the Bloch vector of state $|\psi\rangle$ and that of the initial state $|g\rangle$ on the Bloch sphere. According to the general definition of ergotropy—the maximum work extractable from a quantum state ρ_S under cyclic unitary operations—the ergotropy is given by

$$\mathcal{E} = \mathrm{Tr}[\rho_S H_0] - \min_U \mathrm{Tr}[U\rho_S U^\dagger H_0], \tag{D10}$$

where the minimization is over all unitaries U and the second term is the energy of the corresponding passive state. In the pure state situation, the passive state of ρ_S is $P_{\rho_S} = |g\rangle$, so

$$\begin{aligned}\mathcal{E}(\theta) &= \frac{\omega_q}{2}\left(\sin^2\left(\frac{\theta}{2}\right) - \cos^2\left(\frac{\theta}{2}\right) + 1\right), \\ &= \omega_q \sin^2\left(\frac{\theta}{2}\right), \end{aligned} \tag{D11}$$

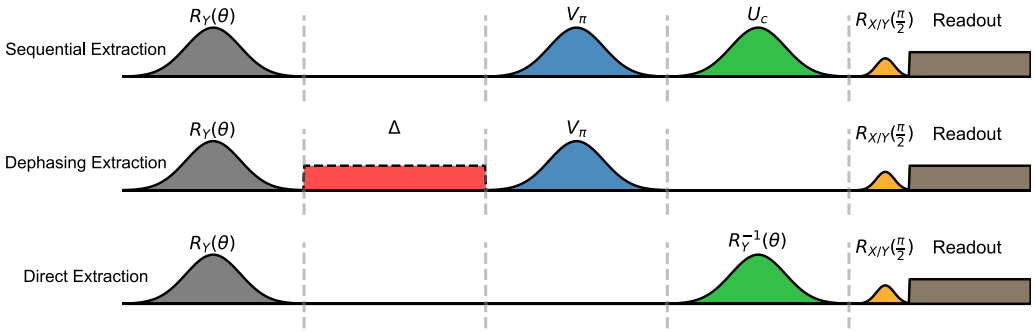


FIG. 11. The pulse sequences for the three types of work extraction are shown. From top to bottom: sequential extraction, dephasing-assisted extraction, and direct extraction.

as shown in Fig. 12(a).

3. $\mathcal{E}_i$ versus Rabi angle

V_π is the optimal coherence-preserving operation that extracts maximum work. The ρ_S is obtained by rotating $|g\rangle$ via the X axis, so V_π can be simply chosen to be rotated via the Y axis for an angle of π, corresponding to an operator of σ_y. The $\mathcal{E}_i$ can be defined as

$$\begin{aligned}\mathcal{E}_i(\theta) &= \mathrm{Tr}[\rho_S H] - \mathrm{Tr}[\sigma_{\rho_S} H] \\ &= \mathrm{Tr}[(\rho_S - \sigma_y \rho_S \sigma_y) H] \\ &= \frac{\omega_q}{2}\left[\sin^2\left(\frac{\theta}{2}\right) - \cos^2\left(\frac{\theta}{2}\right)\right. \\ &\quad \left. - \cos^2\left(\frac{\theta}{2}\right) + \sin^2\left(\frac{\theta}{2}\right)\right] \\ &= -\omega_q \cos(\theta). \end{aligned} \tag{D12}$$

However, according to the definition of V_π, the incoherent ergotropy should remain identically zero for $\theta \leqslant \pi/2$. Therefore,

$$\mathcal{E}_i(\theta) = \begin{cases} 0, & 0 \leqslant \theta \leqslant \frac{\pi}{2}, \\ -\omega_q \cos(\theta), & \frac{\pi}{2} < \theta \leqslant \pi. \end{cases} \tag{D13}$$

4. $\mathcal{E}_c$ versus Rabi angle

From the results of above two sections, we get the form of coherent ergotropy $\mathcal{E}_c = \mathcal{E} - \mathcal{E}_i$

$$\mathcal{E}_c(\theta) = \begin{cases} \omega_q \cos^2\left(\frac{\theta}{2}\right) - \omega_q \cos(\theta), & 0 \leqslant \theta \leqslant \frac{\pi}{2}, \\ \omega_q \sin^2\left(\frac{\theta}{2}\right) + \omega_q \cos(\theta), & \frac{\pi}{2} < \theta < \pi. \end{cases} \tag{D14}$$

5. ΔC during the work extraction cycle

a. Initial state prepared: $|g\rangle \to \rho_S$

According to the definition of C, the ΔC during initial state prepared is

$$\begin{aligned}\Delta C &= C(\rho_S) - C(|g\rangle) \\ &= \mathrm{Tr}\big[\rho_S\big(\log \rho_S - \log \delta_{\rho_S}\big)\big]. \end{aligned} \tag{D15}$$

To calculate the von Neumann entropy, we first point out that $\mathrm{Tr}[\rho \log \rho] \equiv 0$ if ρ is a pure state. Because

$$\begin{aligned}\log \rho &= \sum_i \log \lambda_i |\phi_i\rangle\langle\phi_i|, \\ \rho &= \sum_i \lambda_i |\phi_i\rangle\langle\phi_i|, \end{aligned} \tag{D16}$$

where λ_i is the eigenvalue of ρ, the trace can be written as

$$\begin{aligned}\mathrm{Tr}[\rho \log \rho] &= \sum_j \langle\phi_j| \left[\sum_i \lambda_i \log \lambda_i |\phi_i\rangle\langle\phi_i|\right] |\phi_j\rangle \\ &= \sum_i \lambda_i \log \lambda_i. \end{aligned} \tag{D17}$$

For the pure state density matrix, one have $\lambda_0 = 1, \lambda_{i\geqslant 2} = 0$. Thus, we get

$$\begin{aligned}\mathrm{Tr}[\rho \log \rho] &= \sum_i \lambda_i \log \lambda_i \\ &= 0 \log 0 + 1 \log 1 = 0. \end{aligned} \tag{D18}$$

Then, Eq. (D15) can be calculated as

$$\begin{aligned}\Delta C_{|g\rangle \to \rho_S} &= \mathrm{Tr}\big[\rho_S\big(\log \rho_S - \log \delta_{\rho_S}\big)\big] \\ &= -\mathrm{Tr}\big[\rho_S \log \delta_{\rho_S}\big] \\ &= -\mathrm{Tr}[\rho_S(\log P_e |e\rangle\langle e| + \log P_g |g\rangle\langle g|)] \\ &= -2\sin^2\frac{\theta}{2}\log\left(\sin\frac{\theta}{2}\right) - 2\cos^2\frac{\theta}{2}\log\left(\cos\frac{\theta}{2}\right). \end{aligned}$$

b. Direct extraction: $\rho_S \to |g\rangle$

The ΔC during direct extraction is

$$\begin{aligned}\Delta C_{\rho_S \to |g\rangle} &= -\Delta C_{|g\rangle \to \rho_S} \\ &= 2\sin^2\frac{\theta}{2}\log\left(\sin\frac{\theta}{2}\right) + 2\cos^2\frac{\theta}{2}\log\left(\cos\frac{\theta}{2}\right). \end{aligned}$$

c. Dephasing map: $\rho_S \to \delta_{\rho_S}$

The ΔC after total dephasing is

$$\begin{aligned}\Delta C_{\rho_S \to \delta_{\rho_S}} &= -\Delta C_{|g\rangle \to \rho_S} \\ &= 2\sin^2\frac{\theta}{2}\log\left(\sin\frac{\theta}{2}\right) + 2\cos^2\frac{\theta}{2}\log\left(\cos\frac{\theta}{2}\right). \end{aligned}$$

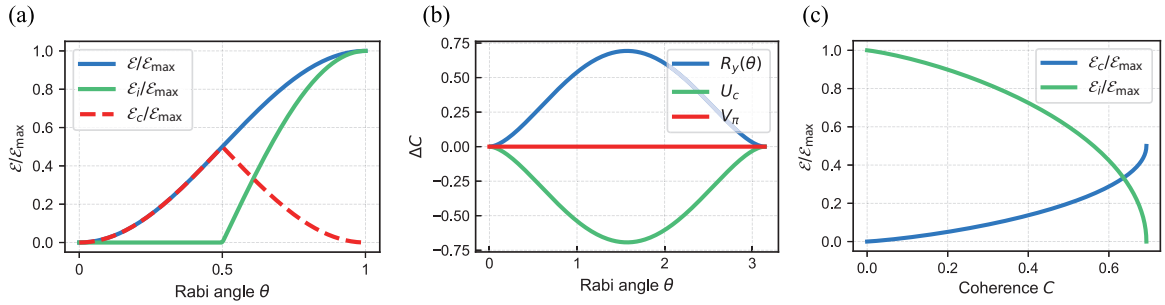


FIG. 12. (a) Dependence of $\mathcal{E}/\mathcal{E}_{\max}$ on the rotation angle θ. (b) Dependence of C on the θ. (c) Dependence of $\mathcal{E}_c/\mathcal{E}_{\max}$ and $\mathcal{E}_i/\mathcal{E}_{\max}$ on the coherence C with the θ varying.

d. Incoherent work extraction: $\rho_S \to \sigma_{\rho_S}$

The ΔC of incoherent work extraction is

$$\begin{aligned}\Delta C_{\rho_S\to\sigma_{\rho_S}} &= \mathrm{Tr}\big[\rho_S\big(\log\rho_S - \log\delta_{\rho_S}\big)\big] \\ &\quad - \mathrm{Tr}\big[\sigma_{\rho_S}\big(\log\sigma_{\rho_S} - \log\delta_{\sigma_{\rho_S}}\big)\big] \\ &= -\mathrm{Tr}\big[\rho_S\log\delta_{\rho_S}\big] + \mathrm{Tr}\big[\sigma_{\rho_S}\log\delta_{\sigma_{\rho_S}}\big] \\ &= 0. \end{aligned} \tag{D19}$$

e. Coherent work extraction: $\rho_S \to \sigma_{\rho_S}$

The ΔC of coherent work extraction is

$$\begin{aligned}\Delta C_{\sigma_{\rho_S}\to P_{\rho_S}} &= -\Delta C_{|g\rangle\to\rho_S} \\ &= \Delta C_{\rho_S\to|g\rangle} \\ &= 2\sin^2\frac{\theta}{2}\log\left(\sin\frac{\theta}{2}\right) + 2\cos^2\frac{\theta}{2}\log\left(\cos\frac{\theta}{2}\right).\end{aligned}$$

Overall, from the above derivation, we see that during the work extraction cycle, the qubit's coherence either remains unchanged or changes by a fixed amount, as shown in Fig. 12(b).

6. $\mathcal{E}_c$ versus C

a. Vary with θ

Because $\mathcal{E}_c$ and C both depend on Rabi angle θ, we can get the relationship between $\mathcal{E}_c$ and C as following. Recall the expression $(\pi/2 \leqslant \theta \leqslant \pi)$

$$C = -2\sin^2\frac{\theta}{2}\log\left(\sin\frac{\theta}{2}\right) - 2\cos^2\frac{\theta}{2}\log\left(\cos\frac{\theta}{2}\right),$$

$$\mathcal{E}_c(\theta) = \omega_q\sin^2\left(\frac{\theta}{2}\right) + \omega_q\cos(\theta), \tag{D20}$$

we introduce

$$x = \sin^2\frac{\theta}{2}, \quad 1-x = \cos^2\frac{\theta}{2}.$$

Then,

$$\begin{aligned}C &= -2\sin^2\frac{\theta}{2}\log\left(\sin\frac{\theta}{2}\right) - 2\cos^2\frac{\theta}{2}\log\left(\cos\frac{\theta}{2}\right) \\ &= -2x\log\sqrt{x} - 2(1-x)\log\sqrt{1-x} \\ &= -x\log x - (1-x)\log(1-x).\end{aligned} \tag{D21}$$

Next, for the ergotropy function

$$\begin{aligned}\mathcal{E}_c(\theta) &= \omega_q\sin^2\frac{\theta}{2} + \omega_q\cos\theta \\ &= \omega_q x + \omega_q(1-2x) \\ &= \omega_q(1-x).\end{aligned} \tag{D22}$$

Solving for x gives

$$x = 1 - \frac{\mathcal{E}_c}{\omega_q}.$$

Substituting back into C yields the explicit relation between C and $\mathcal{E}_c$:

$$\begin{aligned}C &= -x\log x - (1-x)\log(1-x) \\ &= -\left(1-\frac{\mathcal{E}_c}{\omega_q}\right)\log\left(1-\frac{\mathcal{E}_c}{\omega_q}\right) - \frac{\mathcal{E}_c}{\omega_q}\log\left(\frac{\mathcal{E}_c}{\omega_q}\right).\end{aligned} \tag{D23}$$

The way incoherence ergotropy $\mathcal{E}_i$ depends on C can also be obtained by

$$x = \frac{\left(1-\frac{\mathcal{E}_i}{\omega_q}\right)}{2}, \tag{D24}$$

so

$$\begin{aligned}C = &-\frac{\left(1-\frac{\mathcal{E}_i}{\omega_q}\right)}{2}\log\frac{\left(1-\frac{\mathcal{E}_i}{\omega_q}\right)}{2} \\ &-\frac{\left(1+\frac{\mathcal{E}_i}{\omega_q}\right)}{2}\log\frac{\left(1+\frac{\mathcal{E}_i}{\omega_q}\right)}{2}.\end{aligned} \tag{D25}$$

There is no closed-form analytical expression for the relationship between $\mathcal{E}_c$ $(\mathcal{E}_i)$ and C, but it can be plotted numerically, as shown in Fig. 12(c).

We observe that when the contributions from coherent and incoherent ergotropy are equal,

$$\begin{aligned}\omega_q\sin^2\left(\frac{\theta}{2}\right) + \omega_q\cos(\theta) &= -\omega_q\cos(\theta), \\ \cos(\theta) &= -\frac{1}{3}, \\ \theta &= \arccos\left(-\frac{1}{3}\right).\end{aligned} \tag{D26}$$

b. Vary with Δ

In the previous section, we derived the relationship between ergotropy and coherence for pure states on the surface

of the Bloch sphere. In practice, however, mixed states are also of great interest as they highlight the significance of coherence as a quantum resource. We directly replace the off-diagonal elements of the pure-state density matrix with a:

$$\rho_S^{\Delta} = \begin{bmatrix} \sin^2\left(\frac{\theta}{2}\right) & a \\ a^* & \cos^2\left(\frac{\theta}{2}\right) \end{bmatrix}, \tag{D27}$$

where $|a| \leqslant \sin(\frac{\theta}{2})\cos(\frac{\theta}{2})$. Then, the coherence of the state is

$$C_{\rho_S^{\Delta}\to\delta_{\rho_S^{\Delta}}} = \mathrm{Tr}\left[\rho_S^{\Delta}\left(\log\rho_S^{\Delta} - \log\delta_{\rho_S^{\Delta}}\right)\right], \tag{D28}$$

where

$$\delta_{\rho_S^{\Delta}} = \begin{bmatrix} \sin^2\left(\frac{\theta}{2}\right) & 0 \\ 0 & \cos^2\left(\frac{\theta}{2}\right) \end{bmatrix}, \tag{D29}$$

and with the result of Eq. (D18), we can directly get the first term:

$$\begin{aligned} \mathrm{Tr}\left[\rho_S^{\Delta}\log\rho_S^{\Delta}\right] &= \frac{1+R}{2}\log\left(\frac{1+R}{2}\right) \\ &\quad + \frac{1-R}{2}\log\left(\frac{1-R}{2}\right), \\ R &= \sqrt{\cos^2\theta + 4|a|^2}. \end{aligned} \tag{D30}$$

The second term is

$$\begin{aligned} \mathrm{Tr}\left[\rho_S^{\Delta}\log\delta_{\rho_S^{\Delta}}\right] &= \mathrm{Tr}\left[\rho_S^{\Delta}(\log P_e|e\rangle\langle e| + \log P_g|g\rangle\langle g|)\right] \\ &= P_g\log P_g + P_e\log P_e. \end{aligned} \tag{D31}$$

So,

$$\begin{aligned} C = &\frac{1+R}{2}\log\left(\frac{1+R}{2}\right) + \frac{1-R}{2}\log\left(\frac{1-R}{2}\right) \\ &- \left[\sin^2\left(\frac{\theta}{2}\right)\log\sin^2\left(\frac{\theta}{2}\right) + \cos^2\left(\frac{\theta}{2}\right)\log\cos^2\left(\frac{\theta}{2}\right)\right]. \end{aligned}$$

On the other hand, the ergotropy of ρ_S^{Δ} is

$$\mathcal{E} = \frac{\omega_q}{2}(R - \cos\theta), \tag{D32}$$

where we use the eigenvalues to reorder the passive state as

$$\begin{aligned} \rho &= \sum_i p_i|\psi_i\rangle\langle\psi_i|,\ p_1 \geqslant p_2, \\ \rho_P &= p_1|E_0\rangle\langle E_0| + p_2|E_1\rangle\langle E_1|. \end{aligned} \tag{D33}$$

The incoherent part of ergotropy can be obtained by

$$\begin{aligned} \mathcal{E}_i &= E_\rho - E_{\sigma_\rho} \\ &= \mathrm{Tr}[\rho H] - \mathrm{Tr}[\sigma_y\rho\sigma_y H] \\ &= -\omega_q\cos\theta; \end{aligned} \tag{D34}$$

so,

$$\begin{aligned} \mathcal{E}_c &= \mathcal{E} - \mathcal{E}_i \\ &= \frac{\omega_q}{2}(R + \cos\theta). \end{aligned} \tag{D35}$$

The calculation results are shown in Fig. 13, which is also shown in the main text.

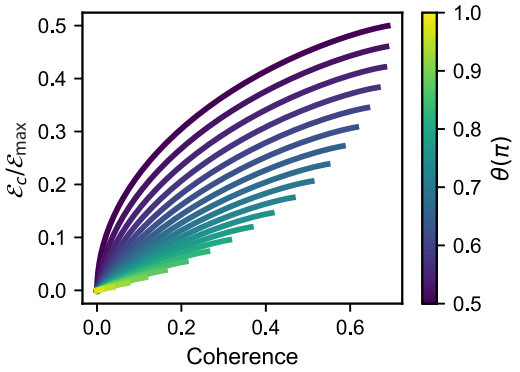


FIG. 13. Dependence of $\mathcal{E}_c/\mathcal{E}_{\max}$ on the coherence C with the fixed θ. It is also shown in the Fig. 1(b).

APPENDIX E: THE THERMODYNAMIC EFFICIENCY

In this section, we focus on the thermodynamic cost and efficiency during the work extraction cycle. According to the definition, the thermodynamic cost during an unitary evolution is ($\hbar = 1$)

$$\Sigma_\tau = \frac{1}{\tau}\int_0^\tau \|H_{\mathrm{int}}(t)\|\mathrm{d}t, \tag{E1}$$

where $\|H_{\mathrm{int}}(t)\| = \sqrt{\mathrm{tr}(H_{\mathrm{int}}^2(t))}$ is the instantaneous Hilbert-Schmidt norm of H_{int}. In the following subsection, we will calculate the thermodynamic cost in different steps.

1. Initial state preparation

The thermodynamic cost during the initial state preparation is dependent on the Rabi angle θ:

$$\begin{aligned} \Sigma_\rho &= \frac{1}{\tau}\int_0^\tau \|g_d V(t)\sigma_x\|\mathrm{d}t \\ &= \frac{1}{\tau}\int_0^\tau g_d V(t)\mathrm{d}t. \end{aligned} \tag{E2}$$

We find that the thermodynamic cost of qubit rotations is proportional to the Rabi angle θ, as $\Sigma_\rho = \theta/\tau$, where $\tau = 80$ ns is a constant. Thus, the thermodynamic efficiency can be calculated as

$$\begin{aligned} \eta_\rho &= \frac{\mathcal{E}_\rho}{\mathcal{E}_\rho + \Sigma_\rho} \\ &= \frac{\omega_q\sin^2(\theta/2)}{\omega_q\sin^2(\theta/2) + \theta/\tau}, \end{aligned} \tag{E3}$$

the results are shown in Fig. 14(a).

On the other hand, we are interested in the relationship between the thermodynamic efficiency of the initial state preparation, the extractable work, and coherence. It can be evaluated by combining the expression of C_ρ and Σ_ρ:

$$\begin{aligned} C_\rho = &-2\sin^2\frac{\theta}{2}\log\left(\sin\frac{\theta}{2}\right) \\ &- 2\cos^2\frac{\theta}{2}\log\left(\cos\frac{\theta}{2}\right) \end{aligned}$$

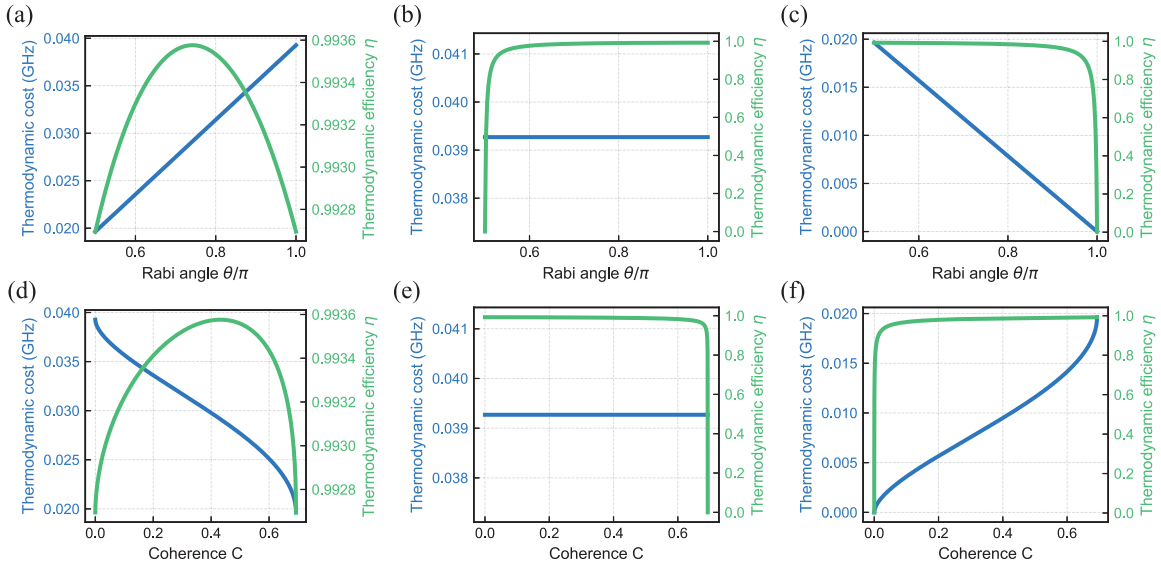


FIG. 14. Thermodynamic cost and efficiency. (a) Dependence of Σ_ρ and η_ρ on the Rabi angle θ. (b) Dependence of Σ_i and η_i on the Rabi angle θ. (c) Dependence of Σ_c and η_i on the Rabi angle θ. (d) Dependence of Σ_ρ and η_ρ on the coherence C. (e) Dependence of Σ_i and η_i on the coherence C. (f) Dependence of Σ_c and η_i on the coherence C.

$$= -2\sin^2\frac{\Sigma_\rho\tau}{2}\log\left(\sin\frac{\Sigma_\rho\tau}{2}\right) - 2\cos^2\frac{\Sigma_\rho\tau}{2}\log\left(\cos\frac{\Sigma_\rho\tau}{2}\right). \tag{E4}$$

This is a transcendental equation, and an analytical expression for the thermodynamic cost as a function of C_ρ remains intractable. However, their relationship can be determined numerically, as shown in Fig. 14(d).

In the interval from $\pi/2$ to π, C is a monotonically decreasing function of θ. As a result, the maxima in Figs. 14(a) and 14(d) correspond to the same point. Numerical calculation yields the corresponding values of θ and C at this point as $\theta_0 = 0.742\pi$ and $C_0 = 0.432$.

2. Incoherent work exaction

The thermodynamic cost and efficiency during the incoherent work extraction step is

$$\Sigma_i = \pi/\tau,$$
$$\eta_i = \frac{\mathcal{E}_i}{\mathcal{E}_i + \Sigma_i} = \frac{-\omega_q\cos(\theta)}{-\omega_q\cos(\theta) + \pi/\tau}. \tag{E5}$$

In contrast to state preparation, the extraction of incoherent ergotropy is governed by a fixed operation, leading to a monotonic dependence of both the thermodynamic cost and efficiency.

3. Coherent work exaction

The thermodynamic cost and efficiency during the coherent work exaction is

$$\Sigma_c = (\pi - \theta)/\tau,$$
$$\eta_c = \frac{\mathcal{E}_c}{\mathcal{E}_c + \Sigma_c} = \frac{\omega_q\cos^2(\theta/2)}{\omega_q\cos^2(\theta/2) + (\pi - \theta)/\tau}. \tag{E6}$$

As shown in Figs. 14(b) and 14(e), in the vicinity of a Rabi angle of π, $\mathcal{E}_c$ drops sharply toward zero, which leads to a pronounced minimum in efficiency close to zero. When $\eta_i = \eta_c$, we get

$$\frac{\omega_q\cos^2(\theta/2)}{\omega_q\cos^2(\theta/2) + (\pi - \theta)/\tau} = \frac{-\omega_q\cos(\theta)}{-\omega_q\cos(\theta) + \pi/\tau}. \tag{E7}$$

The above equation can be rearranged as

$$\left(\frac{3\pi}{2} - \theta\right)\cos\theta + \frac{\pi}{2} = 0. \tag{E8}$$

By solving the above equation numerically, the corresponding root is found to be $\theta_1 = 0.7224\pi$ and $C_1 = 0.469$.

[1] F. Campaioli, S. Gherardini, J. Q. Quach, M. Polini, and G. M. Andolina, *Colloquium*: Quantum batteries, Rev. Mod. Phys. **96**, 031001 (2024).

[2] R. Alicki and M. Fannes, Entanglement boost for extractable work from ensembles of quantum batteries, Phys. Rev. E **87**, 042123 (2013).

[3] P. Skrzypczyk, A. J. Short, and S. Popescu, Work extraction and thermodynamics for individual quantum systems, Nat. Commun. **5**, 4185 (2014).

[4] F. C. Binder, S. Vinjanampathy, K. Modi, and J. Goold, Quantacell: Powerful charging of quantum batteries, New J. Phys. **17**, 075015 (2015).

[5] D. E. Bruschi, M. Perarnau-Llobet, N. Friis, K. V. Hovhannisyan, and M. Huber, Thermodynamics of creating correlations: Limitations and optimal protocols, Phys. Rev. E **91**, 032118 (2015).

[6] F. Campaioli, F. A. Pollock, F. C. Binder, L. Céleri, J. Goold, S. Vinjanampathy, and K. Modi, Enhancing the charging power of quantum batteries, Phys. Rev. Lett. **118**, 150601 (2017).

[7] D. Ferraro, M. Campisi, G. M. Andolina, V. Pellegrini, and M. Polini, High-power collective charging of a solid-state quantum battery, Phys. Rev. Lett. **120**, 117702 (2018).

[8] G. M. Andolina, M. Keck, A. Mari, M. Campisi, V. Giovannetti, and M. Polini, Extractable work, the role of correlations, and asymptotic freedom in quantum batteries, Phys. Rev. Lett. **122**, 047702 (2019).

[9] J.-X. Liu, H.-L. Shi, Y.-H. Shi, X.-H. Wang, and W.-L. Yang, Entanglement and work extraction in the central-spin quantum battery, Phys. Rev. B **104**, 245418 (2021).

[10] L. F. C. Moraes, A. Saguia, A. C. Santos, and M. S. Sarandy, Charging power and stability of always-on transitionless driven quantum batteries, Europhys. Lett. **136**, 23001 (2021).

[11] F.-Q. Dou, Y.-Q. Lu, Y.-J. Wang, and J.-A. Sun, Extended dicke quantum battery with interatomic interactions and driving field, Phys. Rev. B **105**, 115405 (2022).

[12] F.-Q. Dou, H. Zhou, and J.-A. Sun, Cavity Heisenberg-spin-chain quantum battery, Phys. Rev. A **106**, 032212 (2022).

[13] F. Zhao, F.-Q. Dou, and Q. Zhao, Charging performance of the Su-Schrieffer-Heeger quantum battery, Phys. Rev. Res. **4**, 013172 (2022).

[14] B. Mojaveri, R. Jafarzadeh Bahrbeig, M. A. Fasihi, and S. Babanzadeh, Enhancing the direct charging performance of an open quantum battery by adjusting its velocity, Sci. Rep. **13**, 19827 (2023).

[15] J.-Y. Gyhm and U. R. Fischer, Beneficial and detrimental entanglement for quantum battery charging, AVS Quantum Science **6**, 012001 (2024).

[16] P.-R. Lai, J.-D. Lin, Y.-T. Huang, H.-C. Jan, and Y.-N. Chen, Quick charging of a quantum battery with superposed trajectories, Phys. Rev. Res. **6**, 023136 (2024).

[17] W.-L. Song, H.-B. Liu, B. Zhou, W.-L. Yang, and J.-H. An, Remote charging and degradation suppression for the quantum battery, Phys. Rev. Lett. **132**, 090401 (2024).

[18] S. Elghaayda, A. Ali, S. Al-Kuwari, A. Czerwinski, M. Mansour, and S. Haddadi, Performance of a superconducting quantum battery, Adv. Quantum Technol. **8**, 2400651 (2025).

[19] D. Rossini, G. M. Andolina, D. Rosa, M. Carrega, and M. Polini, Quantum advantage in the charging process of Sachdev-Ye-Kitaev batteries, Phys. Rev. Lett. **125**, 236402 (2020).

[20] A. E. Allahverdyan, R. Balian, and T. M. Nieuwenhuizen, Maximal work extraction from finite quantum systems, Europhys. Lett. **67**, 565 (2004).

[21] E. Chitambar and G. Gour, Quantum resource theories, Rev. Mod. Phys. **91**, 025001 (2019).

[22] A. Streltsov, G. Adesso, and M. B. Plenio, *Colloquium* : Quantum coherence as a resource, Rev. Mod. Phys. **89**, 041003 (2017).

[23] K. Korzekwa, M. Lostaglio, J. Oppenheim, and D. Jennings, The extraction of work from quantum coherence, New J. Phys. **18**, 023045 (2016).

[24] G. Francica, J. Goold, and F. Plastina, Role of coherence in the nonequilibrium thermodynamics of quantum systems, Phys. Rev. E **99**, 042105 (2019).

[25] B. Çakmak, Ergotropy from coherences in an open quantum system, Phys. Rev. E **102**, 042111 (2020).

[26] G. Francica, F. C. Binder, G. Guarnieri, M. T. Mitchison, J. Goold, and F. Plastina, Quantum coherence and ergotropy, Phys. Rev. Lett. **125**, 180603 (2020).

[27] H.-L. Shi, S. Ding, Q.-K. Wan, X.-H. Wang, and W.-L. Yang, Entanglement, coherence, and extractable work in quantum batteries, Phys. Rev. Lett. **129**, 130602 (2022).

[28] Z. Niu, Y. Wu, Y. Wang, X. Rong, and J. Du, Experimental investigation of coherent ergotropy in a single spin system, Phys. Rev. Lett. **133**, 180401 (2024).

[29] N. P. de Leon, K. M. Itoh, D. Kim, K. K. Mehta, T. E. Northup, H. Paik, B. S. Palmer, N. Samarth, S. Sangtawesin, and D. W. Steuerman, Materials challenges and opportunities for quantum computing hardware, Science **372**, eabb2823 (2021).

[30] A. A. Clerk, M. H. Devoret, S. M. Girvin, F. Marquardt, and R. J. Schoelkopf, Introduction to quantum noise, measurement, and amplification, Rev. Mod. Phys. **82**, 1155 (2010).

[31] Y. Zheng, S. Campbell, G. De Chiara, and D. Poletti, Cost of counterdiabatic driving and work output, Phys. Rev. A **94**, 042132 (2016).

[32] S. Campbell and S. Deffner, Trade-off between speed and cost in shortcuts to adiabaticity, Phys. Rev. Lett. **118**, 100601 (2017).

[33] O. Abah, R. Puebla, A. Kiely, G. De Chiara, M. Paternostro, and S. Campbell, Energetic cost of quantum control protocols, New J. Phys. **21**, 103048 (2019).

[34] J. Monsel, M. Fellous-Asiani, B. Huard, and A. Auffèves, The energetic cost of work extraction, Phys. Rev. Lett. **124**, 130601 (2020).

[35] T. Baumgratz, M. Cramer, and M. B. Plenio, Quantifying coherence, Phys. Rev. Lett. **113**, 140401 (2014).

[36] J. Koch, T. M. Yu, J. Gambetta, A. A. Houck, D. I. Schuster, J. Majer, A. Blais, M. H. Devoret, S. M. Girvin, and R. J. Schoelkopf, Charge-insensitive qubit design derived from the Cooper pair box, Phys. Rev. A **76**, 042319 (2007).

[37] P. M. Harrington, E. J. Mueller, and K. W. Murch, Engineered dissipation for quantum information science, Nat. Rev. Phys. **4**, 660 (2022).

[38] X. Mi, A. A. Michailidis, S. Shabani, K. C. Miao, P. V. Klimov, J. Lloyd, E. Rosenberg, R. Acharya, I. Aleiner, T. I. Andersen, M. Ansmann, F. Arute, K. Arya, A. Asfaw, J. Atalaya, J. C. Bardin, A. Bengtsson, G. Bortoli, A. Bourassa, J. Bovaird *et al.*, Stable quantum-correlated many-body states through engineered dissipation, Science **383**, 1332 (2024).

[39] L. Li, T. Liu, X.-Y. Guo, H. Zhang, S. Zhao, Z.-A. Wang, Z. Xiang, X. Song, Y.-X. Zhang, K. Xu, H. Fan, and D. Zheng, Observation of multiple steady states with engineered dissipation, npj Quantum Inf. **11**, 2 (2025).

[40] Y. Liang, C. Xie, Z. Guo, P. Huang, W. Huang, Y. Liu, J. Qiu, X. Sun, Z. Wang, X. Yang, J. Zhang, J. Zhang, L. Zhang, J. Chu, W. Guo, J. Jiang, X. Linpeng, S. Liu, J. Niu, Y. Zhou *et al.*, Dephasing-assisted diffusive dynamics in superconducting quantum circuits, Appl. Phys. Lett. **127**, 154003 (2025).

[41] Z. Tao, F. Schmolke, C.-K. Hu, W. Huang, Y. Zhou, J. Zhang, J. Chu, L. Zhang, X. Sun, Z. Guo, J. Niu, W. Weng, S. Liu, Y. Zhong, D. Tan, D. Yu, and E. Lutz, Noise-Induced Quantum

Synchronization with Entangled Oscillations, Nat. Commun. **16**, 8457 (2025).

[42] J. Han, W. Cai, L. Hu, X. Mu, Y. Ma, Y. Xu, W. Wang, H. Wang, Y. P. Song, C.-L. Zou, and L. Sun, Experimental simulation of open quantum system dynamics via trotterization, Phys. Rev. Lett. **127**, 020504 (2021).

[43] J. T. Barreiro, M. Müller, P. Schindler, D. Nigg, T. Monz, M. Chwalla, M. Hennrich, C. F. Roos, P. Zoller, and R. Blatt, An open-system quantum simulator with trapped ions, Nature (London) **470**, 486 (2011).

[44] K. W. Murch, U. Vool, D. Zhou, S. J. Weber, S. M. Girvin, and I. Siddiqi, Cavity-assisted quantum bath engineering, Phys. Rev. Lett. **109**, 183602 (2012).

[45] T. Brown, E. Doucet, D. Ristè, G. Ribeill, K. Cicak, J. Aumentado, R. Simmonds, L. Govia, A. Kamal, and L. Ranzani, Trade off-free entanglement stabilization in a superconducting qutrit-qubit system, Nat. Commun. **13**, 3994 (2022).

[46] T. Liu, S. Liu, H. Li, H. Li, K. Huang, Z. Xiang, X. Song, K. Xu, D. Zheng, and H. Fan, Observation of entanglement transition of pseudo-random mixed states, Nat. Commun. **14**, 1971 (2023).

[47] R. Simmonds, K. Lang, D. Hite, S. Nam, D. Pappas, and J. Martinis, Decoherence in Josephson phase qubits from junction resonators, Phys. Rev. Lett. **93**, 077003 (2004).

[48] J. Lisenfeld, C. Müller, J. H. Cole, P. Bushev, A. Lukashenko, A. Shnirman, and A. V. Ustinov, Measuring the temperature dependence of individual two-level systems by direct coherent control, Phys. Rev. Lett. **105**, 230504 (2010).

[49] J. Lisenfeld, C. Müller, J. H. Cole, P. Bushev, A. Lukashenko, A. Shnirman, and A. V. Ustinov, Rabi spectroscopy of a qubit-fluctuator system, Phys. Rev. B **81**, 100511 (2010).

[50] J. Burnett, L. Faoro, I. Wisby, V. L. Gurtovoi, A. V. Chernykh, G. M. Mikhailov, V. A. Tulin, R. Shaikhaidarov, V. Antonov, P. J. Meeson, A. Ya. Tzalenchuk, and T. Lindström, Evidence for interacting two-level systems from the 1/f noise of a superconducting resonator, Nat. Commun. **5**, 4119 (2014).

[51] P. V. Klimov, J. Kelly, Z. Chen, M. Neeley, A. Megrant, B. Burkett, R. Barends, K. Arya, B. Chiaro, Y. Chen, A. Dunsworth, A. Fowler, B. Foxen, C. Gidney, M. Giustina, R. Graff, T. Huang, E. Jeffrey, E. Lucero, J. Y. Mutus *et al.*, Fluctuations of energy-relaxation times in superconducting qubits, Phys. Rev. Lett. **121**, 090502 (2018).

[52] S. M. Meißner, A. Seiler, J. Lisenfeld, A. V. Ustinov, and G. Weiss, Probing individual tunneling fluctuators with coherently controlled tunneling systems, Phys. Rev. B **97**, 180505 (2018).

[53] D. F. V. James, P. G. Kwiat, W. J. Munro, and A. G. White, Measurement of qubits, Phys. Rev. A **64**, 052312 (2001).

[54] R. T. Thew, K. Nemoto, A. G. White, and W. J. Munro, Qudit quantum-state tomography, Phys. Rev. A **66**, 012303 (2002).

[55] J. Johansson, P. Nation, and F. Nori, Qutip: An open-source python framework for the dynamics of open quantum systems, Comput. Phys. Commun. **183**, 1760 (2012).

[56] J. Johansson, P. Nation, and F. Nori, Qutip 2: A python framework for the dynamics of open quantum systems, Comput. Phys. Commun. **184**, 1234 (2013).

[57] G. S. Uhrig, Keeping a quantum bit alive by optimized π-pulse sequences, Phys. Rev. Lett. **98**, 100504 (2007).

[58] Ł. Cywiński, R. M. Lutchyn, C. P. Nave, and S. D. Sarma, How to enhance dephasing time in superconducting qubits, Phys. Rev. B **77**, 174509 (2008).

[59] J.-M. Cai, B. Naydenov, R. Pfeiffer, L. P. McGuinness, K. D. Jahnke, F. Jelezko, M. B. Plenio, and A. Retzker, Robust dynamical decoupling with concatenated continuous driving, New J. Phys. **14**, 113023 (2012).

[60] X. Xu, Z. Wang, C. Duan, P. Huang, P. Wang, Y. Wang, N. Xu, X. Kong, F. Shi, X. Rong, and J. Du, Coherence-protected quantum gate by continuous dynamical decoupling in diamond, Phys. Rev. Lett. **109**, 070502 (2012).

[61] Q. Guo, S.-B. Zheng, J. Wang, C. Song, P. Zhang, K. Li, W. Liu, H. Deng, K. Huang, D. Zheng, X. Zhu, H. Wang, C.-Y. Lu, and J.-W. Pan, Dephasing-insensitive quantum information storage and processing with superconducting qubits, Phys. Rev. Lett. **121**, 130501 (2018).

[62] K. C. Miao, J. P. Blanton, C. P. Anderson, A. Bourassa, A. L. Crook, G. Wolfowicz, H. Abe, T. Ohshima, and D. D. Awschalom, Universal coherence protection in a solid-state spin qubit, Science **369**, 1493 (2020).

[63] Z. Huang, P. S. Mundada, A. Gyenis, D. I. Schuster, A. A. Houck, and J. Koch, Engineering dynamical sweet spots to protect qubits from $1/f$ noise, Phys. Rev. Appl. **15**, 034065 (2021).

[64] S. Deffner, Energetic cost of Hamiltonian quantum gates, Europhys. Lett. **134**, 40002 (2021).

[65] C.-K. Hu, J. Qiu, P. J. P. Souza, J. Yuan, Y. Zhou, L. Zhang, J. Chu, X. Pan, L. Hu, J. Li, Y. Xu, Y. Zhong, S. Liu, F. Yan, D. Tan, R. Bachelard, C. J. Villas-Boas, A. C. Santos, and D. Yu, Optimal charging of a superconducting quantum battery, Quantum Sci. Technol. **7**, 045018 (2022).

[66] Y. Ge, X. Yu, W. Xin, Z. Wang, Y. Zhang, W. Zheng, S. Li, D. Lan, and Y. Yu, Efficient charging and discharging of a superconducting quantum battery through frequency-modulated driving, Appl. Phys. Lett. **123**, 154002 (2023).

[67] Z. Lin, L. Zhang, X. Long, Y.-a. Fan, Y. Li, K. Tang, J. Li, X. Nie, T. Xin, X.-J. Liu, and D. Lu, Experimental quantum simulation of non-Hermitian dynamical topological states using stochastic Schrödinger equation, npj Quantum Inf. **8**, 77 (2022).

[68] R. Barends, J. Kelly, A. Megrant, D. Sank, E. Jeffrey, Y. Chen, Y. Yin, B. Chiaro, J. Mutus, C. Neill, P. O'Malley, P. Roushan, J. Wenner, T. C. White, A. N. Cleland, and J. M. Martinis, Coherent Josephson qubit suitable for scalable quantum integrated circuits, Phys. Rev. Lett. **111**, 080502 (2013).

[69] L. Li, S.-L. Zhao, Y.-H. Shi, B.-J. Chen, X. Ruan, G.-H. Liang, W.-P. Yuan, J.-C. Song, C.-L. Deng, Y. Liu, T.-M. Li, Z.-H. Liu, X.-Y. Guo, X. Song, K. Xu, H. Fan, Z. Xiang, and D. Zheng, Stable and efficient charging of superconducting C-shunt flux quantum batteries, Phys. Rev. Appl. **24**, 054033 (2025).